



3D GROUND MOTION SIMULATIONS FOR EVENTS IN THE 2019 RIDGECREST SEQUENCE

R. Graves⁽¹⁾, A. Pitarka⁽²⁾

⁽¹⁾ Research Geophysicist, U.S. Geological Survey, rwgraves@usgs.gov

⁽²⁾ Seismologist, Lawrence Livermore National Laboratory, pitarka1@llnl.gov

Abstract

The main goals of this work are to test the adequacy of existing Southern California Earthquake Center (SCEC) 3D Community Velocity Models (CVMs) in simulating long period ($T > 1$ sec) ground motions for events in the Ridgecrest sequence, and to examine features of the CVMs that impact their ability to fit the observed motions. Ultimately, the hope is to develop a well-calibrated and validated 3D velocity model for the Ridgecrest region that can then be used for detailed source analyses of the larger events in the 2019 sequence.

In addition to the M6.4 and M7.1 events, the Ridgecrest sequence produced several moderate magnitude (\sim M5) earthquakes that were also well-recorded by the roughly 300 stations of the Southern California Seismic Network (SCSN). Using these data, we examine the adequacy of existing Southern California Earthquake Center (SCEC) 3D Community Velocity Models (CVMs) to simulate long period ($T > 1$ sec) ground motions across southern California. Preliminary analysis of the long period motions from moderate magnitude events at sites in the epicentral area show very simple waveforms, indicating that these events can be treated as point sources and that the subsurface structure near these sites is relatively simple. Further to the south in the Los Angeles region, the recorded motions exhibit significant amplification (factors of 3-4) and long shaking durations for sites within the deep basins as compared to sites located outside of the basins. In Ridgecrest and across the Mojave Desert, both SCEC CVMs (CVM-H and CVM-SI) are comprised of smoothly varying velocity structure that is constrained primarily by waveform tomography. To the south, this structure transitions into several deep low-velocity basins in the Los Angeles region; however, the details of these structures differ somewhat between the two CVMs. In the first phase of our work, we simulate the long-period motions for the moderate magnitude events using both CVMs, and assess the ability of each model to reproduce the observed motions at sites across the southern California region. In the second phase, we extend our analysis to the M7.1 mainshock in order to explore our ability to capture both complex finite-faulting effects along with 3D wave propagation effects.

Keywords: 2019 Ridgecrest Earthquakes; Strong Ground Motion; 3D Modeling; Seismic Velocity Structure



1. Introduction

The July 2019 Ridgecrest earthquake sequence occurred on a complex set of faults within the eastern California shear zone. The largest events in the sequence were a moment magnitude (M_w) 6.4 foreshock having a left-lateral slip mechanism, which was followed about 34 hours later by the M_w 7.1 right-lateral mainshock. These largest events both produced surface rupture and occurred on a conjugate set of fault segments [1]. This type of conjugate faulting is similar to what occurred previously in the Salton Sea region of southern California during the 1987 Superstition Hills sequence [2].

The sequence produced numerous events including over 70 with magnitude greater than 4.0 in the first 3 weeks. Ross et al. [3] performed a systematic relocation of the seismicity and along with insights from remote sensing produce a detailed analysis of the kinematics of the earthquake sequence. They found that events in the sequence occurred on multiple sets of orthogonal faults across the entire rupture zone. Additionally, their analysis was able to map out the spatio-temporal progression of seismicity between the M_w 6.4 and M_w 7.1 events, including the occurrence of an M_w 5.4 event about 16 hours before the M_w 7.1 mainshock (see Fig. 1).

A large number of the events in the sequence were recorded by the more than 300 instruments of the Southern California Seismic Network (SCSN), including at 15 sites located within about 40 km of the ruptures (Fig. 1). Data from these near-fault recording sites provide useful constraints on the evolution of the rupture process during the M_w 7.1 mainshock [3,4,5]. These studies (and others) determined that the mainshock traversed multiple fault segments with a relative slow rupture velocity (~ 2 km/s) and consisted of at least four main subevents. Parker et al [6] utilized the SCSN data along with observations from other seismic networks to compare with an empirical ground motion model (GMM) in order to analyze source, path and site effects across southern California. They found the empirical GMM was able to match the median ground motion levels across a range of periods for $M > 4$ events in the sequence. Additionally, they found strong amplification of motions for periods greater than 1 s at sites in the deep sedimentary basins of Los Angeles and Ventura that were not fully captured by the empirical GMM.

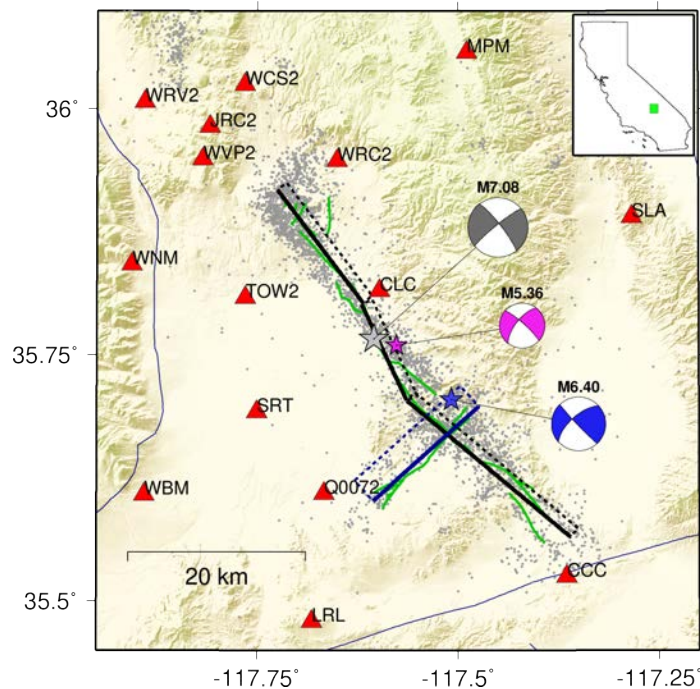


Fig. 1 – Map of the Ridgecrest region showing the locations and mechanisms of the three largest events in the 2019 sequence. Mapped surface ruptures [1] (green lines), nearby recording sites (red triangles), and one month of seismicity (small gray circles) also shown. The blue and black rectangles denote the surface projections of fault planes used to simulate the M_w 6.4 and M_w 7.1 events, respectively.



In this paper we begin with an analysis of the recorded motions for the M_w 5.4 event paying particular attention to the observed response in the Los Angeles (LA) basin region. We then model these data using existing SCEC 3D Community Velocity Models (CVMs) in order to benchmark the models' performance over the period range 1 – 10 s. We then shift our focus to modeling the ground motions for the M_w 7.1 mainshock. This component of the study additionally requires the development of a suitable finite-fault rupture model, which is done using the Graves-Pitarka method [7]. In the final section, we summarize our results and discuss possible ways that the models might be improved for future work.

2. M_w 5.4 Observations

The M_w 5.4 event (SCSN ID: 38450263) occurred about 16 hours prior to the M_w 7.1 mainshock with an epicenter about 2 km southeast of the mainshock epicenter (Fig. 1). The focal mechanism of this event is quite similar to the mainshock mechanism and indicates primarily strike-slip faulting along either a NW-SE or SW-NE striking fault. Ground motions from this event were recorded throughout southern California with high quality data recovered out to epicentral distances beyond 300 km. Fig. 2 shows the distribution of stations that we analyze in our study.

The radial and tangential component ground velocity waveforms for the M_w 5.4 event at stations located along a profile extending southward from the Ridgecrest area across the LA basin (green triangles in Fig. 2) are displayed in Fig. 3. These waveforms have been low-pass filtered at $f < 1$ Hz. The amplitude of the motions decays roughly as expected out to an epicentral distance of about 190 km where the motions begin to increase in amplitude as they enter the LA basin. Amplification of the motions in the basin continues until the waves reach the deepest portion of the basin (site LTP) and then the amplitude decreases as the waves exit the basin to the south (site RPV). At these lower frequencies, the relative amplification of the motions within the basin is about a factor of 3-4 compared to motions at sites outside the basin.

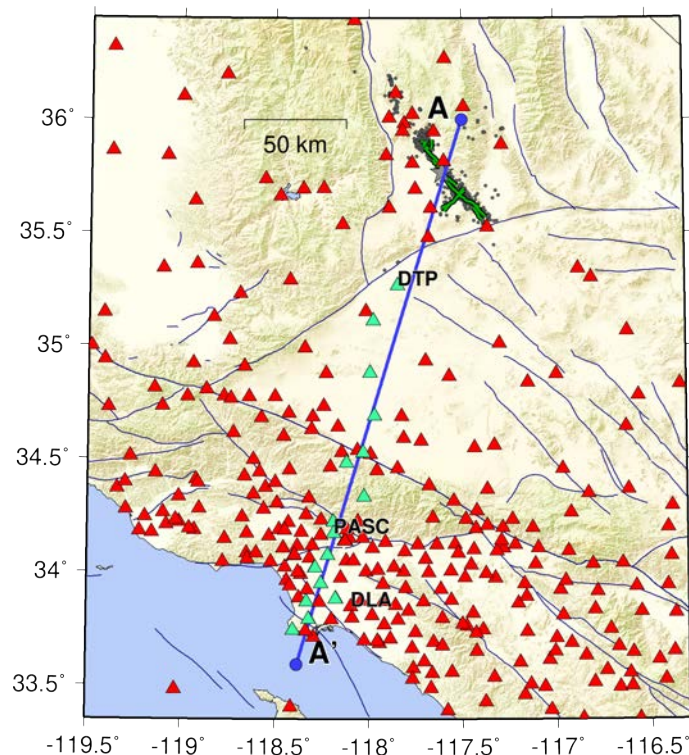


Fig. 2 – Map of the southern California region extending from the Ridgecrest source area in the north to the Los Angeles area in the south. The red and green triangles are SCSN sites that recorded the M_w 5.4 and M_w 7.1 events. Indicated stations along profile A-A' are discussed further in the main text.

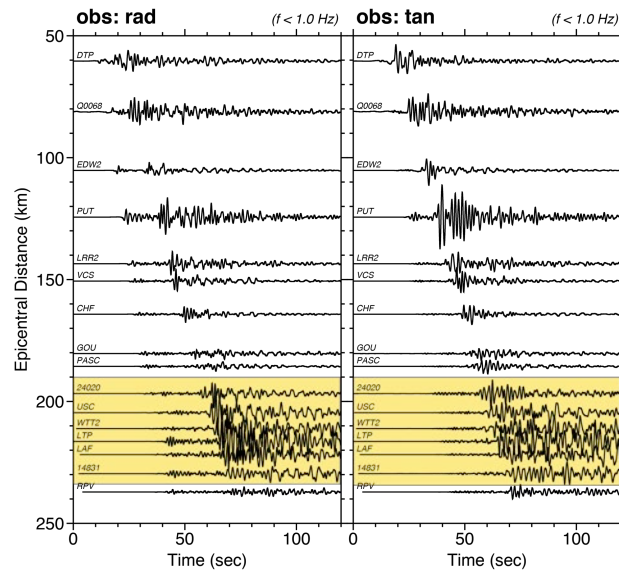


Fig. 3 – Profiles of recorded radial (left) and tangential (right) ground velocity waveforms ($f < 1$ Hz) for the M_w 5.4 event. Stations run roughly north to south and are indicated by the light green triangles in Fig. 2. The location of the LA basin along the profile is denoted by the yellow shading.

3. 3D Seismic Velocity Models

The data described in the previous section provide an excellent opportunity to examine the adequacy of the SCEC 3D CVMs in modeling the observed amplification within the LA basin. We consider two versions of the CVMs: CVM-S4.26.M01 [8] (CVM-SI hereafter) and CVM-H15.10.0 [9] (CVM-H hereafter).

In CVM-SI, the initial basin structure is constrained using a rule-based seismic velocity model, derived primarily from well log data, where seismic velocity is a function of sediment age and depth. In CVM-H, basin structures are determined from sonic logs and seismic reflection profiles collected by the petroleum industry. The models are further refined using tomographic inversions with a variety of data sets including earthquakes, ambient noise correlation, seismic reflection profiles and receiver functions. Both models utilize a high-resolution geotechnical layer (GTL) based primarily on V_{s30} values to represent the upper few hundred meters of the model; however, the implementation of the GTL is slightly different in each model.

Fig. 4 shows shear wave velocity cross sections from the two models taken along the profile A-A'. Most of the region covered by these cross sections lies in the background portions of the models where the seismic

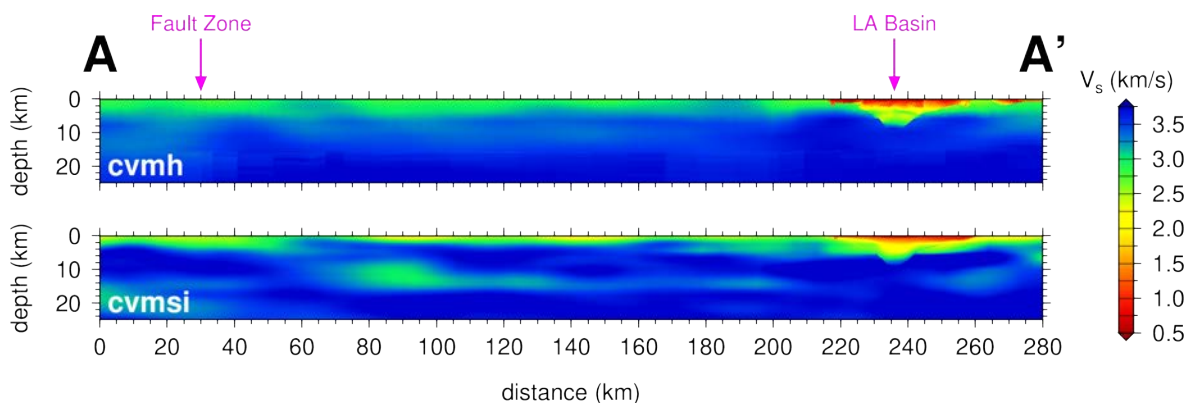


Fig. 4 – Shear wave velocity cross sections for the two CVMs along profile A-A'.



velocity structure is controlled by waveform tomography inversions. Hence, the velocity variations are very smooth both laterally and vertically. The LA basin is located at the southern end of the profile, and the basin structure is clearly evident in both models. Even at this scale, some differences are apparent in the representation of the LA basin in the two models. In CVM-H the general basin structure is more sharply defined compared to CVM-SI, and furthermore, CVM-H contains several lateral discontinuities in the basin velocity structure that are not seen in CVM-SI. Another difference in the models is the velocity gradient as a function of depth within the basin. CVM-H has relatively lower velocities than CVM-SI in the upper 1-2 km of the basin; however, these increase with depth more rapidly such that CVM-H has somewhat higher velocities around 2-5 km depth compared to CVM-SI. Below about 5 km depth, the basin velocities are similar for the two models.

These models are considered adequate for modeling ground motions at periods about 5 s and longer. At shorter periods, the performance of the models begins to decrease, although they are still able to capture many of the general trends and features seen in observed ground motion data [10].

4. M_w 5.4 Simulations

Given the long period bandwidth we are investigating, the M_w 5.4 event can be treated as point source in our simulations models. The hypocenter is: lon.= -117.5645, lat.= 35.7589, depth= 7.5 km, and the focal mechanism is: strike= 314, dip= 81, rake= -165. Since the velocity structure is slightly different at the source location for the two CVMs, we normalize the source strength such that the seismic potency (slip x fault area) is the same in both simulations. This results in slightly different magnitudes for the two models, but is the proper approach when comparing ground motion amplitudes. Using the 3D finite difference method, we generate synthetics accurate down to 1 s period (5 grid points per minimum shear wavelength) for the 3D CVMs using a minimum shear wave velocity (V_s) of 500 m/s and a 100 m grid spacing. Anelastic attenuation is modeled using the relations $Q_s = 50V_s$ (for V_s in km/s) and $Q_p = 2Q_s$.

Fig. 5 displays profiles of simulated radial and tangential component motions for the same set of stations as shown for the observations in Fig. 3. Just as was done with the observations, these motions have been low-pass filtered at $f < 1$ Hz. Both sets of simulations show the same general trend of amplification in the LA basin regions as is seen in the observations. Comparing the two simulations, we see that the radial component

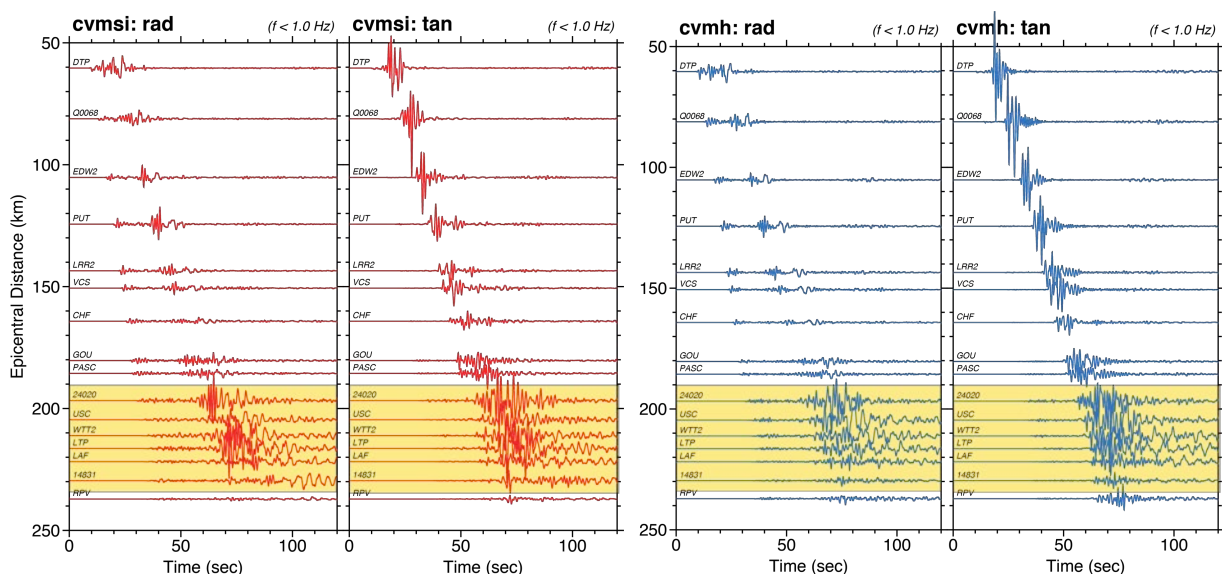


Fig. 5 – Profiles of simulated radial and tangential ground velocity waveforms for the M_w 5.4 event using CVM-SI (left panels) and CVM-H (right panels). Other labeling is same as Fig. 3.



motions for sites in the LA basin using the CVM-SI model are larger than those for CVM-H, whereas the opposite is true for the tangential component. This can be traced back to the strength of the tangential motions coming into the basin, which are noticeably larger for CVM-H compared to CVM-SI. We suspect that this results from more efficient trapping of SH waves in the upper few hundred meters of the CVM-H model due to the lower seismic velocities in the background GTL as compared to CVM-SI.

In order to gain some insight into the behavior of the motions in different frequency bands, we plot three-component waveform comparisons between the observations and simulations in Fig. 6 at three selected sites in the passbands $f < 0.2$ Hz, $f < 0.3$ Hz, and $f < 1$ Hz. The sites are DTP (Mojave desert region), PASC (just north of LA basin), and DLA (deep LA basin), which are indicated on the map in Fig. 2. At the lowest frequency passband ($f < 0.2$ Hz), the agreement between the simulations and the observed records is very good both in terms of amplitude and phasing. The most noticeable mismatch occurs late in the records for the deep basin site (DLA). This is consistent with the result of Taborda et al [10] who found the CVMs performed well at these low frequencies.

Moving to higher frequency passbands, we see that the waveform fits are not as well matched as they are for the lower frequencies. In some ways this is expected since the waveform tomography updates to the CVMs are limited to $f < 0.2$ Hz. Thus, they do not contain well-resolved deterministic features at the length scales need to closely match the amplitude and phasing of the waveforms at higher frequencies. Nonetheless, the match to the observations is still relatively good at $f < 0.3$ Hz. Furthermore, in a more general sense, the simulations do well at matching the overall amplitude and character of the observations, even if they do not closely match the exact phasing at the higher frequency passbands.

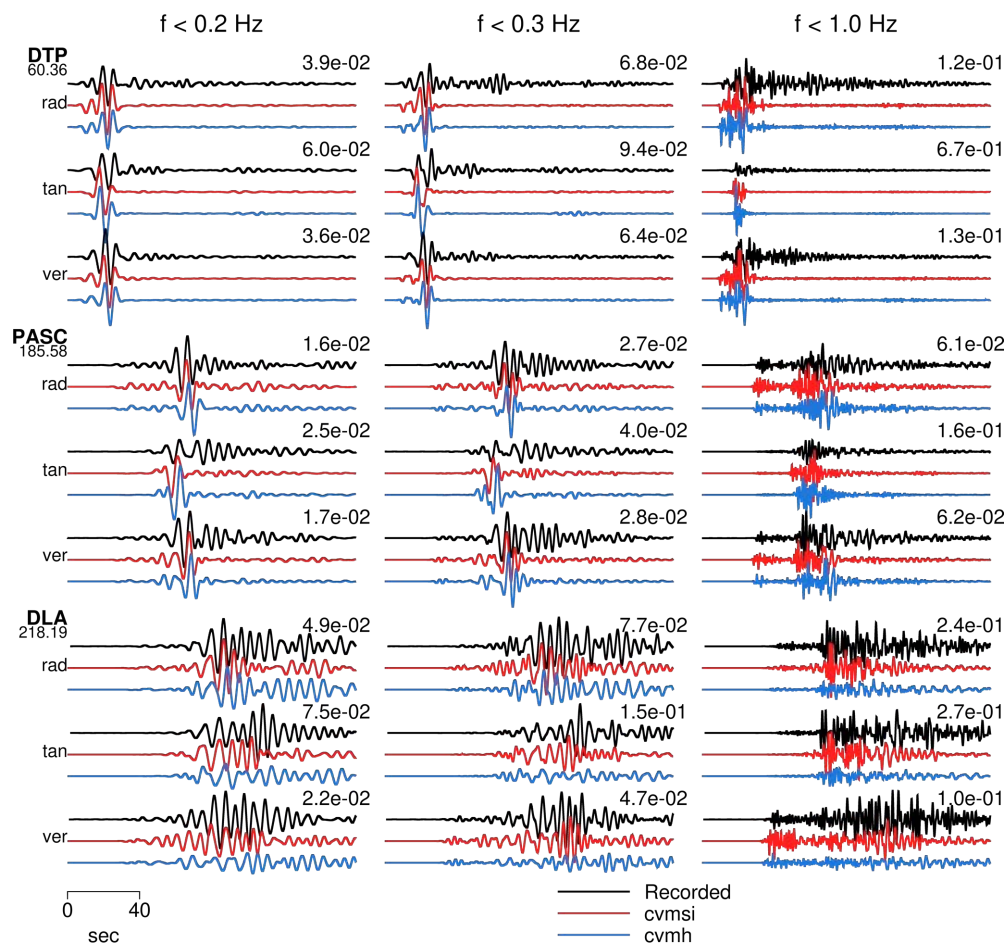


Fig. 6 – Comparison of M_w 5.4 observed and simulated ground velocity waveforms event at three selected sites in the passbands $f < 0.2$ Hz (left), $f < 0.3$ Hz (middle) and $f < 1$ Hz (right). Peak values (cm/s) shown above traces.



In order to provide a more quantitative assessment of the models' performance, we use the response spectral acceleration Goodness-of-Fit (GoF) criterion of Goulet et al. [11]. This is determined by first computing 5%-damped RotD50 [12] response spectral acceleration for all observed and simulated horizontal component motions. For each site j , we then compute the residual as a function of period T_i in the log domain

$$r_j(T_i) = \ln[O_j(T_i)/S_j(T_i)], \quad (1)$$

where O_j and S_j are the observed and simulated responses, respectively. The model bias is then given by

$$B(T_i) = \frac{1}{N} \sum_{j=1,N} r_j(T_i) \quad (2)$$

and the standard deviation is given by

$$\sigma(T_i) = \left\{ \frac{1}{N} \sum_{j=1,N} [r_j(T_i) - B(T_i)]^2 \right\}^{1/2} \quad (3)$$

where N is the total number of stations. In computing the response spectral acceleration metrics we only consider periods (T_i) that are at least 50% higher than the shortest reliable period of the simulation (T_s). Given $T_s = 1$ s, we get $T_i > 1.5$ s.

Fig. 7 shows the model bias and standard deviation for the M_w 5.4 simulations in the two CVMs for three separate distance bins: 0 – 50 km (Ridgecrest region), 50 – 170 km (Mojave Desert region), and 170 – 300 km (LA basin region). For the 0 – 50 km bin, CVM-SI provides a good match to the observations over the full period range, with a slight underprediction (positive bias) centered about 4 s. In this same distance bin, CVM-H shows overprediction (negative bias) for periods less than 3 s; however, for longer periods this model exhibits near zero bias out to 9 s. The standard deviation is similar for the two models in this distance bin and ranges from about 0.6 to 0.8 natural log units. For the 50 – 170 km bin, the results for the two models are quite

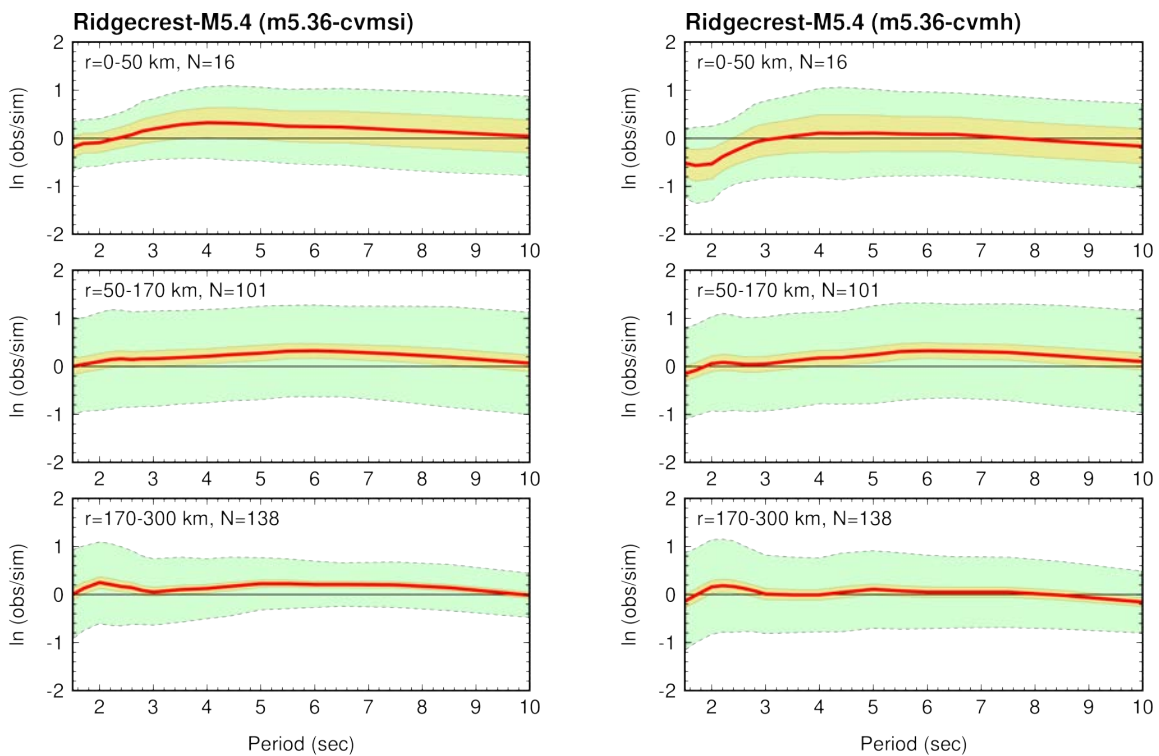


Fig. 7 – RotD50 GoF comparisons for M_w 5.4 simulations in CVM-SI (left) and CVM-H (right). Model bias is shown by red line, yellow shading is 90% confidence interval of the mean, and green shading is standard deviation. Distance bins are 0 – 50 km (top row), 50 – 170 km (middle row) and 170 – 300 km (bottom row). Number of stations (N) in each bin also indicated.



similar. Both show slight underprediction of about 20% centered around 6 s period. The standard deviation is similar for the two models at about 1.0 natural log units across the full period range.

For the 170 – 300 km bin, which contains many of the LA basin sites, CVM-SI produces a slight underprediction (positive bias) across most periods while CVM-H has near zero bias except for small underprediction below 3 s and small overprediction above 9 s. It is interesting that both models show a small positive peak in the bias (underprediction) around 2 s period. Given the distance from the source and the fact that this feature does not appear in the other distance bins, we suspect that this might be due to some common characteristic of the basin structure shared by the two models. Another interesting feature in this distance bin is the difference in standard deviation for the two models: CVM-SI ranges from about 0.6 at short periods to about 0.4 at longer periods, whereas CVM-H ranges from about 0.8 to 0.6 across the period band. This means that although CVM-SI slightly under predicts the median bias, the variability in matching the observations is significantly less compared to CVM-H. This may result from differences in the waveform tomography updates used in the models.

The results of the above comparisons indicate that both CVM-SI and CVM-H do reasonably well in matching the general characteristics of the response in the LA basin region for events occurring in the Ridgecrest region. CVM-SI appears to be better at matching the phasing of the waveforms (as indicated by the lower s) and CVM-H appears to be better at matching the median response level (as indicated by the near-zero bias).

5. M_w 7.1 Mainshock Simulations

Our primary goal in modeling the M_w 7.1 mainshock is to assess the capabilities of the Graves-Pitarka (GP) [7] kinematic rupture generator to produce ruptures that can capture the main characteristics of the observed ground motion response. The GP approach creates ruptures from randomized spatial fields having a magnitude dependent correlation structure. Additionally, the GP approach allows for fault roughness and spatially variable rupture speed and rise time, each of which may be partially correlated with the slip distribution. Obviously these randomized ruptures cannot match the specific details of the Ridgecrest earthquake; however, we hope to be able to generate ruptures that when used in simulations produce relatively low bias and standard deviation when compared to the observed ground motions.

Based on analysis of available kinematic source inversions [4,5], we decided to use a 52 km long, three-segment fault for the M_w 7.1 rupture (see Fig. 1). Each segment dips 85 degrees to the east and the average rake is 180 degrees. Previous analyses [3,4,5] suggest that most of the fault slip occurred shallower than about 12 – 15 km and the rupture had a relatively slow average propagation velocity. To sample these distributions in our simulations, we generated a suite of ruptures using a range of down-dip rupture widths from 13 – 16 km along with average rupture speeds ranging from 50 – 70% of the local shear wave speed. Given space constraints, we only show results here from the rupture model that produced the lowest overall GoF bias, which is plotted in Fig. 8. This rupture has a width of 14 km and average rupture speed of 65% of the local V_s .

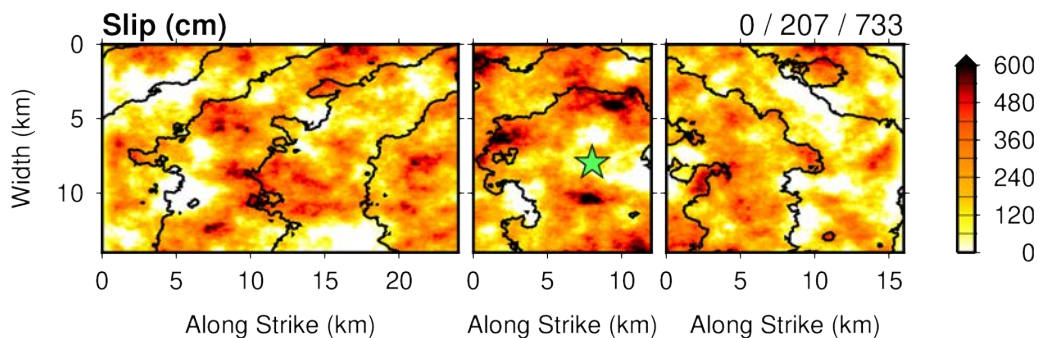


Fig. 8 – Plot of slip distribution (color shading) and 3 second interval rupture time contours (black lines) for best-fitting GP rupture model. Hypocenter shown by green star with minimum/average/maximum slip at upper right.



Fig. 9 plots the RotD50 GoF results for M_w 7.1 simulations in the two CVMs using the rupture model shown in Fig. 8. In general, both models do well in matching the median level of motions across the full range of periods and distances. These results also show some of the same trends seen in the M_w 5.4 GoF results, such as a tendency for slight overprediction at the shorter periods and slight underprediction at longer periods. For the Ridgecrest (0 – 50 km) and Mojave (50 – 170 km) regions, the GoFs for the two models are quite similar for periods greater than about 5 s. At shorter periods in these regions the median level of the CVM-H motions are relatively higher (more negative bias) compared to the CVM-SI motions. As was seen with the M_w 5.4 simulations, we suspect this results from more efficient trapping of short period waves in the upper few hundred meters of the CVM-H model due to the lower seismic velocities in the background GTL as compared to CVM-SI. These same trends are also evident in the LA basin region (170 – 300 km), although the bias of the CVM-H motions has a larger negative shift (about 0.2 natural log units) relative to CVM-SI, meaning that the median level of LA basin motions in CVM-H is about 20 – 25% higher compared with CVM-SI. This difference is likely due to the relatively lower seismic velocities in the upper 1 – 2 km of the basin sediments in CVM-H compared to CVM-SI (see Fig. 4).

For the other rupture models we tested (not shown for brevity), variations in rupture width and rupture speed affect the response in generally systematic ways. We find that decreasing the rupture width (increasing static stress drop) or increasing the rupture speed (increasing corner frequency) generally results in higher ground motion levels across all periods. While these general trends will likely be true across a range of ruptures, the details of the response will obviously depend on the specific features of the rupture realizations and slip distributions.

In Fig. 10, we plot three-component waveform comparisons between the observations and M_w 7.1 simulations using the rupture model in Fig. 8 at three selected sites in the passbands $f < 0.2$ Hz, $f < 0.3$ Hz, and $f < 1$ Hz. The sites are DTP (Mojave desert region), PASC (just north of LA basin), and DLA (deep LA basin),

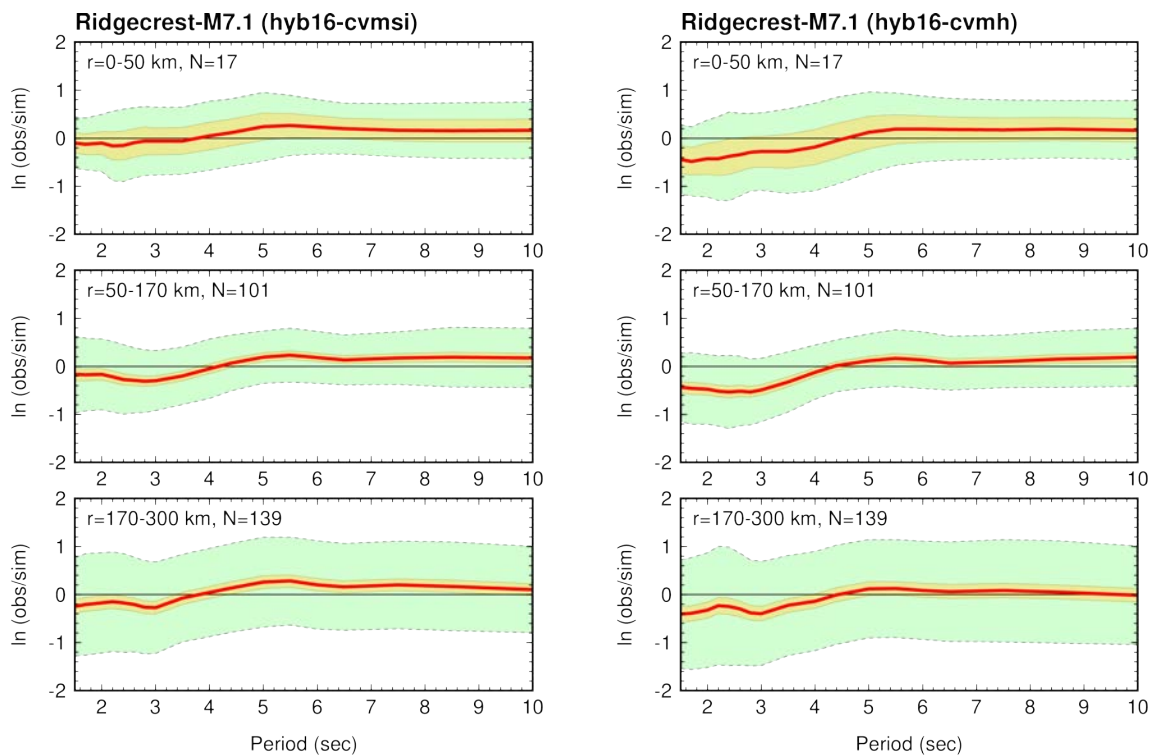


Fig. 9 – RotD50 GoF comparisons for M_w 7.1 simulations in CVM-SI (left) and CVM-H (right). Model bias is shown by red line, yellow shading is 90% confidence interval of the mean, and green shading is standard deviation. Distance bins are 0 – 50 km (top row), 50 – 170 km (middle row) and 170 – 300 km (bottom row). Number of stations (N) in each bin also indicated.



which are the same sites used for the M_w 5.4 results shown in Fig. 6. Given the stochastic nature of the rupture model, we do not expect to match the details of the observed waveforms. Nonetheless, the simulations are able to capture some of the main amplitude and duration features of the records. As noted previously, the two simulations are quite similar for sites outside of the LA basin (DTP and PASC). Additionally, the match to the vertical motions is very good for these sites across all bandwidths. The horizontal motions are not matched as well, suggesting that there are some unmodeled aspects of the rupture that more strongly affect the horizontal radiation pattern compared to the vertical.

The motions within the basin (DLA) are not matched as well as the non-basin sites, and furthermore the response for the two models exhibit notable differences in the waveform phasing particularly at the higher frequencies. In many ways this is not surprising given the differences in the basin structure of the CVMs and the differences seen in the simulated response for the M_w 5.4 event (Fig. 6). That said, the simulations do capture the general amplitude level, duration and character of the observations, even if they do not exactly reproduce the phasing of the recorded motions.

6. Conclusions

The Ridgecrest earthquake sequence produced about ten events in the magnitude range 4.9 – 7.1, and these events were large enough to be well recorded by SCSN instruments throughout southern California. These data provide an excellent opportunity to examine the performance of both 3D seismic velocity models (CVMs)

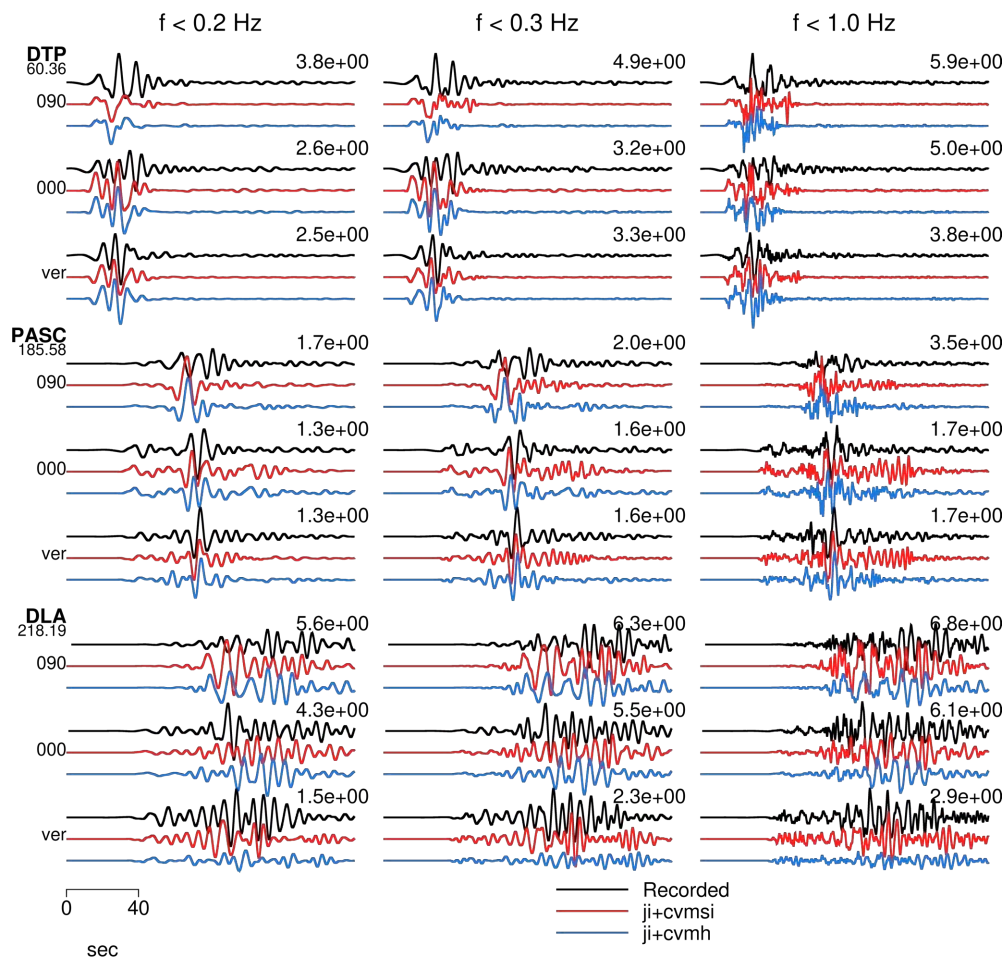


Fig. 10 – Comparison of M_w 7.1 observed and simulated ground velocity waveforms event at three selected sites in the passbands $f < 0.2$ Hz (left), $f < 0.3$ Hz (middle) and $f < 1$ Hz (right).



and finite-fault rupture characterization. As a first step in this study, we use moderate magnitude events to examine the performance of the velocity models. This is attractive because the source can typically be represented as a point moment-tensor for periods above 1 s., which allows us to better understand the behavior of the CVMs without the complications of finite-fault rupture effects. Given acceptable results from the point source modeling, the analysis can then be extended to modeling the larger, finite-fault ruptures of the sequence.

In our modeling of the M_w 5.4 event, we find that both CVM-SI and CVM-H perform well in reproducing the amplitude and phasing of observed motions at periods greater than about 4 – 5 s. At shorter periods, the models still do well in capturing the general amplitude level of the motions; however, they are not able to deterministically match the detailed phasing of the observed waveforms. For sites in the LA basin, both models predict amplification of motions that is generally consistent with the observed motions. The amplification seen in CVM-H is slightly higher than for CVM-SI due to the relatively lower seismic velocities in the upper 1 – 2 km used in the basin sediments of CVM-H.

Extending our analysis to the M_w 7.1 mainshock we are able to generate a stochastic finite-fault rupture model that produces relatively low bias compared to observations for sites across the Mojave region and into the LA basin. We see relatively small differences between the M_w 7.1 simulations for CVM-SI and CVM-H at sites in the Ridgecrest and Mojave region; however, just as with the M_w 5.4 simulations, the models produce more noticeable differences for sites in the LA basin. Even though our rupture characterization procedure is not able to reproduce the specific details of the actual M_w 7.1 rupture, we are still encouraged by its overall positive performance. Furthermore, we recognize that the results presented here are just one step in the validation process of numerical ground motion simulations. Each earthquake presents new challenges, but through this modeling process we can build confidence in using our rupture generator and 3D CVMs in forward simulation exercises for future earthquakes.

7. Acknowledgements

The authors thank Elizabeth Cochran and Art Frankel for providing constructive reviews that helped improve the manuscript. Waveform data from the Southern California Seismic Network (SCSN) were obtained from the Southern California Earthquake Data Center (SCEDC) [13]. SCSN and SCEDC are cooperative projects of Caltech and the U.S. Geological Survey. The authors acknowledge the Texas Advanced Computing Center (TACC) at The University of Texas at Austin (<http://www.tacc.utexas.edu>) for providing high performance computing resources through an allocation to the Southern California Earthquake Center (SCEC). All of the figures were made using Generic Mapping Tools (GMT) version 4.5.3 (<http://www.soest.hawaii.edu/gmt>) [14].

8. References

- [1] Kendrick K, Akciz S, Angster S, Avouac J, Bachhuber J, Bennett S, Blake K, Bork S, Brooks B, Burgess P, Chupik C, Dawson T, DeFrisco M, Delano J, DeLong S, Dolan J, DuRoss C, Erickson T, Frost E, Gold R, Graehl N, Haddon E, Hatem A, Hernandez J, Hitchcock C, Hudnut K, Koehler R, Kozaci O, Ladinsky T, Madugo C, Mareschal M, McPhillips D, Milliner C, Morelan A, Nevitt J, Olson B, Padilla S, Patton J, Philibosian B, Pickering A, Pierce I, Ponti D, Pridmore C, Rosa C, Roth N, Scharer K, Seitz G, Spangler E, Swanson B, Thomas K, Thompson-Jobe J, Treiman J, Williams A, Oskin M (2019): Geologic observations of surface fault rupture associated with the Ridgecrest M6.4 and M7.1 earthquake sequence by the Ridgecrest Rupture Mapping Group, *Abstract 217*, 2019 SCEC Annual Meeting.
- [2] Hudnut K, Seeber L, Pacheco J (1989): Cross - fault triggering in the November 1987 Superstition Hills Earthquake Sequence, southern California. *Geophysical Research Letters*, doi:10.1029/GL016i002p00199.
- [3] Ross Z, Idini B, Jia Z, Stephenson O, Zhong M, Wang X, Zhan Z, Simons M, Fielding E, Yun S, Hauksson E, Moore A, Liu Z, Jung J (2019): Hierarchical interlocked orthogonal faulting in the 2019 Ridgecrest earthquake sequence. *Science*, 10.1126/science.aaz0109.
- [4] Ji C, Archuleta R, Tsuda K, Condon S (2019): Preliminary seismological analyses of 2019 Mw 6.4 Searles Valley and Mw 7.1 Ridgecrest California earthquakes, *Abstract 259*, 2019 SCEC Annual Meeting.



- [5] Dreger D, Wang K, Tinti E, Burgmann R, Taira T (2019): Rupture History of the July 4 and July 6 2019 Ridgecrest Earthquakes, *Abstract S31G-0494*, 2019 AGU Fall Meeting.
- [6] Parker G, Baltay A, Rekoske J, Thompson E (2020): Repeatable Source-, Path-, and Site-Effects from the 2019 Ridgecrest M7.1 Earthquake Sequence, *submitted to Bull. Seism. Soc. Am.*
- [7] Graves R, Pitarka A (2016): Kinematic ground motion simulations on rough faults including effects of 3D Stochastic velocity perturbations, *Bull Seis. Soc Am.*, **106**, 2136–2153, doi:10.1785/0120160088.
- [8] Lee E, Chen P, Jordan T, Maechling P, Denolle M, Beroza G (2014): Full-3-D tomography for crustal structure in southern California based on the scattering-integral and the adjoint-wavefield methods. *Journal of Geophysical Research: Solid Earth*, **119**(8), 6421–6451, doi:10.1002/2014JB011346.
- [9] Shaw J, Plesch A, Tape C, Suess M, Jordan T, Ely G, Hauksson E, Tromp J, Tanimoto T, Graves R, Olsen K (2015): Unified structural representation of the southern California crust and upper mantle. *Earth and Planetary Science Letters*, **415**, 1-15, doi:10.1016/j.epsl.2015.01.016.
- [10] Taborda R, Azizzadeh-Roodpish S, Khoshnevis N, Cheng K (2016): Evaluation of the southern California seismic velocity models through simulation of recorded events. *Geophysical Journal International*, **205**(3), 1342-1364, doi:10.1093/gji/ggw085.
- [11] Goulet C, Abrahamson N, Somerville P, Wooddell K (2015): The SCEC Broadband Platform validation exercise for pseudo-spectral acceleration: Methodology for code validation in the context of seismic hazard analyses, *Seismological Research Letters*, **86**(1), 17–26, doi:10.1785/0220140104.
- [12] Boore D (2010): Orientation-independent, non geometric-mean measures of seismic intensity from two horizontal components of motion, *Bull. Seismol. Soc. Am.* **100**, 1830–1835, doi:10.1785/0120090400.
- [13] SCEDC (2013): Southern California Earthquake Data Center. Caltech. Dataset. doi:10.7909/C3WD3xH1.
- [14] Wessel P, Smith W (1998): New, improved version of generic mapping tools released, *Eos Trans. AGU* **79**, **47**, 579–579, 10.1029/98EO00426.